Proceedings of the Combustion Institute 42 (2026) 106836

Contents lists available at ScienceDirect

Proceedings of the Combustion Institute

journal homepage: www.elsevier.com/locate/proci

ZND-guided low-dimensional manifold sampling for artificial-neural-network-accelerated simulation of oblique detonation

Tinghao Wang [b], Qizhe Wen [b], Jie Sun [b], John Z. Ma [b], Zhi X. Chen [b], Zhi-Qin John Xu [c], Tianhan Zhang [a,d,*], Jianping Wang [b], Zheng Chen [b]

[a] School of Astronautics, Beihang University, Beijing, 100191, China
[b] CCSE, SKLTCS, HEDPS, School of Mechanics and Engineering Science, Peking University, Beijing, 100871, China
[c] Institute of Natural Sciences, School of Mathematical Sciences, Shanghai Jiao Tong University, Shanghai, 200240, China
[d] Key Laboratory of Spacecraft Design Optimization and Dynamic Simulation Technologies, Beijing, 102206, China

ARTICLE INFO

Keywords:
Chemical source term
Neural network
Surrogate model
Numerical simulation
Oblique detonation

ABSTRACT

Numerical simulations of detonation are crucial for advancing detonation engine development, yet the computation of chemical source terms remains a primary efficiency bottleneck. Artificial neural networks (ANNs) offer promising surrogate models, but their accuracy hinges on a critical and understudied step: how the high-dimensional thermochemical space is sampled to generate training data. Existing strategies such as multi-scale sampling, though effective across a wide range of combustion scenarios, are not tailored to the strongly correlated states that arise in detonation. This study introduces a sampling method built on a physical low-dimensional manifold defined by the one-dimensional Zeldovich–von Neumann–Döring (ZND) structure, combined with data augmentation, to efficiently populate the thermochemical space without resorting to costly two-dimensional simulations. In the cases examined, ZND-manifold-based sampling produced more accurate posteriori predictions than the multi-scale baseline at the same dataset size, suggesting that physically informed manifolds provide an effective basis for sampling in detonation simulations. Built on this dataset, the ANN framework supports variable time steps, allowing a single trained network to operate across different conditions. Separate networks trained for H_2/air, $C_2H_2/O_2/Ar$, and RP3/air reproduce oblique detonation wave (ODW) initiation over a range of operating conditions, with predicted thermodynamic fields and key parameters (e.g., ODW angle) in close agreement with the conventional CVODE integrator. The trained networks also reduce the chemical source-term cost by 3× (CPU) and 17× (GPU) for H_2/air and by up to 7.5× (CPU) and 83× (GPU) for the larger RP3/air mechanism. These results demonstrate that ZND-guided low-dimensional manifolds provide a robust and efficient sampling foundation for complex detonation surrogates, with potential extensions to broader detonation applications.

Novelty and significance statement: This work introduces a low-dimensional manifold approach based on one-dimensional Zeldovich–von Neumann–Döring (ZND) structures to generate training datasets for two-dimensional oblique detonation simulations. A high-pressure augmentation strategy is developed to capture thermochemical states in ODW initiation. The ZND-guided sampling strategy avoids costly multi-dimensional CFD simulations while covering the thermochemical space relevant to oblique detonation wave (ODW) phenomena. Trained on this dataset, the proposed artificial neural network (ANN) reproduces the thermodynamic fields and wave structures of ODW initiation while reducing the chemical source-term cost, for example by 17× on GPUs for H_2/air. In an ablation study for the present ODW case, low-dimensional-manifold-based sampling produced more accurate posteriori predictions than the multi-scale baseline at the same number of samples, suggesting that physically informed manifolds can improve sampling efficiency for the detonation simulations considered here. To the best of the authors' knowledge, this is the first application of ANNs to accelerate chemical source-term computation in ODW simulations.

* Corresponding author at: School of Astronautics, Beihang University, Beijing, 100191, China.
E-mail address: thzhang@buaa.edu.cn (T. Zhang).

https://doi.org/10.1016/j.proci.2026.106836
Received 15 March 2026; Accepted 26 June 2026
Available online 4 November 2026
1540-7489/© 2026 The Combustion Institute. Published by Elsevier Inc. All rights are reserved, including those for text and data mining, AI training, and similar technologies.

1. Introduction

Detonation offers a compelling approach for aerospace propulsion owing to its high thermodynamic efficiency and compactness [1]. Among detonation-based propulsion concepts, the oblique detonation engine (ODE) [2] has emerged as a leading candidate for flight above Mach 10 due to its unique shock-compression-to-detonation structure that enables efficient supersonic combustion within a compact combustor. However, the strong coupling between the supersonic inflow and the detonation wave introduces complex physical processes that pose significant challenges for numerical simulation. Experimental observations reveal that oblique detonation waves (ODWs) exhibit a two-zone configuration consisting of initiation and stabilization regions [3], which is not captured by simplified one-dimensional models [4]. Through two-dimensional simulations, Teng et al. [5] investigated the transition from an oblique shock wave (OSW) to an ODW and classified it into two types: smooth and abrupt. These findings underscore the complexity of ODW phenomena and emphasize the need for advanced multi-dimensional numerical simulation tools.

In detonation simulations, accurately resolving turbulent and supersonic flow fields is only part of the challenge; the computation of chemical source terms also poses a significant bottleneck. The extremely short chemical time scales lead to severe stiffness in the governing ordinary differential equations (ODEs), and chemical reactions are tightly coupled with the complex flow field, further increasing the dimensionality of the thermochemical state space. Detailed chemical mechanisms are essential for accurately resolving the ODW initiation structure [5,6], yet traditional stiff ODE solvers (e.g., CVODE) can account for roughly 70%–85% of the total computing time depending on the case (see Table 2), constituting the primary computational bottleneck.

Artificial neural networks (ANNs) represent one of the most promising approaches to accelerate chemical source-term evaluation. Christo et al. [7] first proposed using ANNs to replace direct time integration for chemical source terms. Over the past decades, researchers have focused on several key aspects: sampling methods [8–13], neural network architectures [14–16], and enforcement of physical conservation laws [11,17]; interested readers are referred to the comprehensive review by Ihme et al. [18]. Despite the growing adoption of neural networks in combustion simulations, research targeting supersonic combustion — particularly detonation scenarios — remains limited. In existing detonation studies, ANNs are mainly used for predicting detonation cell size [19] and flow-field reconstruction [20], whereas work on using ANNs to accelerate chemical source-term evaluation in detonation simulations remains scarce. As a data-driven approach, the quality and representativeness of the training dataset are paramount. Constructing an effective dataset for two-dimensional detonation problems is particularly challenging: the most straightforward strategy — sampling directly from two-dimensional simulations — incurs prohibitive computational cost, severely limiting coverage of the broad operating parameter space and raising concerns about model generalizability. Recent studies have shown that the Zeldovich–von Neumann–Döring (ZND) structure provides an efficient low-dimensional manifold for generating representative detonation data to simulate two-dimensional cellular detonation without repeated multi-dimensional simulations [21]. Chen et al. [22] successfully solved the one-dimensional shock tube problem using samples generated from a one-dimensional shock tube setup. Barwey et al. [23] investigated a linearized model detonation engine (LMDE) and discussed the potential benefits of clustering techniques, such as k-means, for ANN-based simulations. However, their dataset was still obtained from two-dimensional LMDE simulations. Nevertheless, it remains unclear whether the ZND-guided framework is applicable to two-dimensional oblique detonation scenarios and, if so, how this low-dimensional manifold corresponding to one-dimensional detonation can be effectively combined with ANNs to yield a robust and efficient surrogate model for chemical source terms.

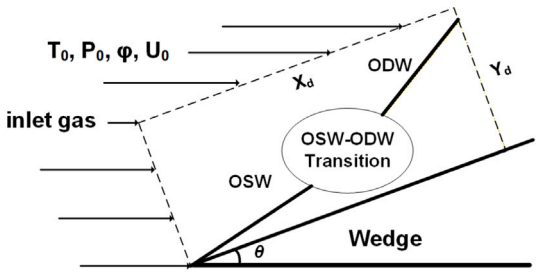


Fig. 1. Computational configuration.

This study explores the use of a ZND-guided low-dimensional manifold to develop an efficient sampling strategy and a corresponding ANN surrogate for chemical source terms in detonation simulations. Section 2 details the ANN-based framework, including the sampling strategy, network architecture, training procedure, and inference implementation within the CFD solver. Section 3 assesses the accuracy and computational efficiency of the proposed approach by comparing it with the conventional CVODE integrator in two-dimensional ODW simulations for H_2/air, $C_2H_2/O_2/Ar$, and RP3/air mixtures. Moreover, an ablation study is conducted to compare low-dimensional-manifold-based sampling with direct sampling in the high-dimensional thermochemical space for H_2/air mixtures. Finally, conclusions and directions for future research are discussed (see Fig. 2).

2. Methodology

2.1. Computational configuration

Fig. 1 shows the computational configuration for ODW initiation: a uniform, unburned premixed inflow impinges on a wedge, inducing a transition from an OSW to an ODW through chemical reactions.

The wedge angle θ and inlet gas conditions (T_0, P_0, φ, U_0) are chosen following Teng et al. [5] and Zhang et al. [24], as summarized in Table 1. Cases 1 and 2 correspond to the working conditions at an altitude of 30 km with Mach numbers of 8 and 10, respectively [5]. For $C_2H_2/O_2/Ar$ mixtures, we follow Zhang et al. [24], in which the pre-compression process in ODE inlets was not considered. The inlet Mach numbers for Cases 3 and 4 are 7 and 10, respectively. The inflow conditions of Case 5 follow those of Case 2. The computational domain dimensions X_d and Y_d are set according to the inlet conditions, with a no-slip wall on the wedge surface, inflow boundaries on the left and top, and an outflow boundary on the right.

All simulations are performed using `dfHighSpeedFoam` in DeepFlame [25], which supports both CVODE and ANN for chemical source-term evaluation. Time integration employs a first-order Euler scheme, and convective fluxes are computed using the Tadmor scheme with a TVD limiter. The simulation proceeds in two stages: first, a steady OSW is established with chemical reactions disabled; subsequently, chemical reactions are activated to evolve the flow toward the steady ODW initiation structure.

Two technical challenges arise when applying neural networks to ODW initiation problems. The first is the wide variation in time step across different operating conditions. Because the induction length changes dramatically with post-shock temperature, X_d, Y_d, the grid resolution, and the time step can vary by over an order of magnitude across cases. If the neural network is trained for a fixed time step Δt, it is restricted to specific inlet conditions and lacks generality. Equipping the neural network with variable time-step capability is therefore essential. The second challenge is the complexity of the ODW initiation thermochemical space. The ODW initiation process involves multiple

Table 1
Working conditions of ODW initiation in this work.

Case No.	Mixtures	θ	T_0 (K)	P_0 (kPa)	φ	U_0 (m/s)	Transition type
1	H_2/air	19°	742.8	32.5	1.0	2188.2	Abrupt
2		19°	972.1	54.3	1.0	2757.6	Smooth
3	C_2H_2/O_2/Ar	25°	298.15	20.3	1.0	2228.6	Abrupt
4		25°	298.15	20.3	1.0	3183.8	Smooth
5	RP3/air	19°	972.1	54.3	1.0	2757.6	Abrupt

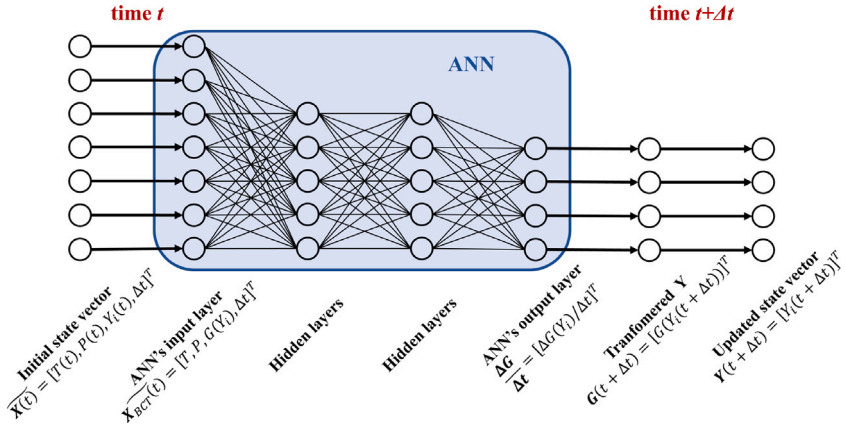


Fig. 2. Neural network structure.

interacting wave structures — including the OSW, compression waves, Mach stems, and reflected shocks — each of which produces distinct thermochemical states. The training dataset must adequately cover this broad and complex state space to ensure reliable ANN predictions.

2.2. Neural network-based framework

This section describes the neural network architecture designed to accommodate variable time steps Δt.

The governing equations solved by `dfHighSpeedFoam` can be written in compact form as

$$\frac{\partial \rho}{\partial t} + \nabla \cdot (\rho \mathbf{u}) = 0, \tag{1}$$

$$\frac{\partial (\rho \mathbf{u})}{\partial t} + \nabla \cdot (\rho \mathbf{u}\mathbf{u}) = -\nabla p + \nabla \cdot \boldsymbol{\tau}, \tag{2}$$

$$\frac{\partial (\rho Y_\alpha)}{\partial t} + \nabla \cdot (\rho \mathbf{u} Y_\alpha) = -\nabla \cdot (\rho Y_\alpha \mathbf{V}_\alpha) + \dot{\omega}_\alpha, \tag{3}$$

$$\frac{\partial (\rho E)}{\partial t} + \nabla \cdot [\mathbf{u}(\rho E + p)] = \nabla \cdot (\boldsymbol{\tau} \cdot \mathbf{u}) - \nabla \cdot \mathbf{q}, \tag{4}$$

where ρ, $\mathbf{u}$, p, Y_α, $\dot{\omega}_\alpha$, and E denote the mixture density, velocity, pressure, mass fraction of species α, net production rate of species α, and total energy, respectively. Here, the total energy is defined as $E = e + \frac{1}{2}|\mathbf{u}|^2$, with e being the internal energy. The chemical source terms $\dot{\omega}_\alpha$ are used to update the species composition, rather than to directly solve for temperature or pressure. The temperature and pressure are obtained jointly from the total energy equation and the equation of state based on the updated thermochemical state. Therefore, the ANN introduced in this work replaces the chemistry integration step, while the flow and thermodynamic variables remain coupled through the governing equations in `dfHighSpeedFoam`.

The neural network replaces direct integration of the chemical source term, which depends on reaction rates and the thermochemical state. The mixture state is defined as $\mathbf{X} = [T, P, Y_1, \ldots, Y_n]^\mathsf{T}$, where T is the temperature, P is the pressure, and Y_i $(i = 1, \ldots, n)$ are the species mass fractions. Let $\mathbf{Y} = [Y_1, \ldots, Y_n]^\mathsf{T}$. The source term is governed by the ODE system:

$$\frac{\dot{\omega}_\alpha}{\rho} = \frac{dY_\alpha}{dt} = f_\alpha(\mathbf{X}). \tag{5}$$

The neural network is designed to predict $\mathbf{Y}(t + \Delta t)$ from the current state $\mathbf{X}(t)$ and the variable time step Δt employed in the numerical simulation.

Neural networks with variable time steps have been explored in ChemNODE [15], DeepONets [16], and related studies. In this work, we extend the framework of Zhang et al. [10] by incorporating Δt as an additional input and develop an end-to-end neural surrogate that maps $\mathbf{X}(t)$ and Δt to $\mathbf{Y}(t + \Delta t)$. Defining the augmented input vector $\widetilde{\mathbf{X}}(t) = [T(t), P(t), Y_1(t), \ldots, Y_n(t), \Delta t]^\mathsf{T}$, the network mapping can be expressed as:

$$\mathbf{Y}_{ANN}(t + \Delta t) = \mathcal{F}\left(\widetilde{\mathbf{X}}(t)\right), \tag{6}$$

where $\mathcal{F}$ represents the nonlinear function parameterized by the neural network. The ANN predictions of chemical source terms are

$$\dot{\omega}_{\alpha,ANN} = \rho \frac{Y_{\alpha,ANN}(t + \Delta t) - Y_\alpha(t)}{\Delta t}. \tag{7}$$

To accommodate species mass fractions spanning multiple orders of magnitude, the Box–Cox transformation [26] is applied to the output quantities. The dataset is split into 90%/10% partitions for training and validation, respectively. Separate neural networks are trained for the three fuel systems listed in Table 1. For H_2/air and C_2H_2/O_2/Ar mixtures, a single neural network is employed for both the abrupt and smooth ODW initiation cases.

2.3. Sampling strategy

Building on the framework outlined in Section 2.2, we construct a dataset of thermochemical states $\mathbf{X}$ that comprehensively spans the thermochemical space encountered in ODWs. As noted in Section 1, the dataset is derived from computationally tractable one-dimensional (1D) and zero-dimensional (0D) problems, avoiding the need for expensive two-dimensional (2D) ODW simulations. For given T_0, P_0, and φ, the data generation procedure consists of five steps. Taking the conditions of Case 1 as an example, the procedure is detailed below.

Step 1: ZND Profile Sampling. Cantera [27] and SDToolbox [28] are employed to compute one-dimensional ZND solutions. In the direction normal to the ODW front, the governing equations reduce to those

of a normal detonation:

$$\dot{m} = \rho_0 u_{0n} = \rho_1 u_{1n} \tag{8}$$

$$p_0 + \rho_0 u_{0n}^2 = p_1 + \rho_1 u_{1n}^2 \tag{9}$$

$$\frac{\gamma}{\gamma-1}\frac{p_0}{\rho_0} + q + \frac{1}{2}u_{0n}^2 = \frac{\gamma}{\gamma-1}\frac{p_1}{\rho_1} + \frac{1}{2}u_{1n}^2 \tag{10}$$

where subscript 0 denotes upstream conditions and 1 denotes the post-shock state. The normal velocity is $u_{0n} = U_0 \sin\beta$, where U_0 is the inflow velocity and β is the angle between the inflow and the wavefront. To cover the OSW, ODW, and transition structures, ZND solutions are computed for normal velocities from 1200 to 2100 m/s in 20 m/s increments. For velocities at or above the Chapman–Jouguet speed, classical ZND structures are obtained; for sub-CJ velocities, solutions feature decoupled shock and reaction zones.

Step 2: High-Pressure Augmentation. Complex 2D wave structures can produce pressures and temperatures exceeding those in 1D ZND solutions [5]. To address this, we perform numerical augmentation: (i) compute $k = (P - P_0)/(T - T_0)$ and determine its range $[k_{\min}, k_{\max}]$ from the ZND dataset; (ii) for each sample $\mathbf{X} = [T, P, Y_1, \ldots, Y_n]^\mathsf{T}$, generate five new samples $\mathbf{X}' = [T, P', Y_1, \ldots, Y_n]^\mathsf{T}$ where $(P' - P_0)/(T - T_0) \in [k_{\min}, k_{\max}]$. This extends coverage to high-pressure regions associated with Mach stems.

Step 3: Low-Temperature Autoignition Sampling. Ideally, unburned gas remains inert upstream of the shock; however, finite-rate chemistry and shock thickness necessitate sampling in low-temperature /low-pressure regimes. Given negligible diffusion in detonations and correlated species fractions during H_2/air autoignition, we simulate isochoric autoignition (using Cantera) at initial conditions $T = 1100$ K, $P = 1$ atm, and $\varphi = 1$, yielding 100 species composition vectors $\mathbf{Y}$. These are combined with $T \in [950, 1500]$ K (10 points) and $P \in [0.3, 2]$ atm (10 points), producing 10,000 data points relevant to ODW initiation.

Step 4: Perturbation-Based Augmentation. We apply perturbation schemes from prior work [25,29] to enhance dataset diversity. The detailed formulas for the perturbation method are provided in the references mentioned above. In this work, the key parameter, i.e., the perturbation rate ε, is set to 0.05.

Step 5: Multi-Time-Step Augmentation. For each $\mathbf{X}(t)$ generated in the preceding four steps, multiple values of $\Delta t \in [8\times10^{-10}, 1.2\times10^{-8}]$ s are randomly sampled to construct a set of augmented inputs $\widetilde{\mathbf{X}}(t)$. Training labels $\mathbf{Y}(t + \Delta t)$ are generated via zero-dimensional isochoric reactors in Cantera, and the neural network is trained following the procedure described in Section 2.2. In practical applications, the trained ANN can remain accurate even when Δt slightly exceeds the sampling range, but such extrapolation should be limited. A detailed discussion is provided in Appendix C.

Fig. 3 presents phase diagrams comparing the sampled thermochemical states with reference ODW initiation data obtained using `dfHighSpeedFoam` with CVODE (gray points). The diagrams plot temperature (x-axis) against Y_{OH} (y-axis). In Fig. 3(a), colored curves represent ZND solutions computed via Cantera for normal velocities ranging from 1200 to 2100 m/s. These span most of the ODW thermochemical space but exclude two key regions: (i) a high-temperature, high-pressure zone associated with the Mach stem during abrupt OSW–ODW transitions, and (ii) the low-temperature regime. These gaps are addressed by Step 2 (high-pressure augmentation) and Step 3 (low-temperature autoignition sampling). Fig. 3(b) compares the final augmented dataset (orange points) with the reference ODW data (gray points). All reference states lie within the envelope of the sampled data, confirming that the ZND-based dataset comprehensively covers the thermochemical space of the two-dimensional ODW initiation problem.

When the operating conditions (T_0, P_0, φ) differ across cases, multiple values of these quantities are selected to cover the relevant range of working conditions. The computational cost of the entire sampling workflow is minimal (less than one CPU-hour), making it straightforward to generate and merge multiple datasets.

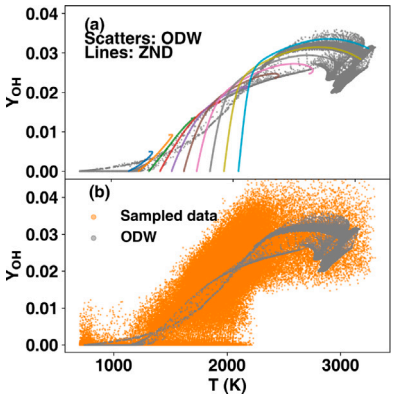


Fig. 3. Phase diagrams comparing (a) original ZND-sampled data with ODW reference data, and (b) final augmented dataset with ODW reference data.

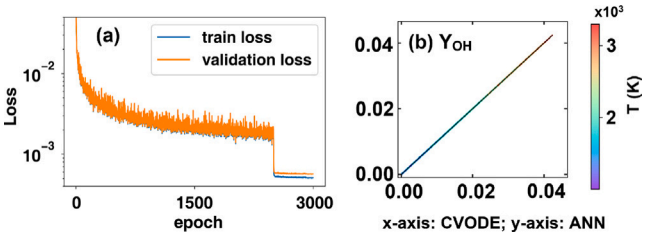


Fig. 4. (a) Evolution of training and validation loss during the training process; (b) one-step Y_{OH} predictions: Cantera reference (x-axis) vs. ANN prediction (y-axis) on the validation dataset.

3. Results and discussion

3.1. H_2/Air mixtures

For H_2/air mixtures, the chemistry is modeled using the Burke mechanism [30], reduced to 9 species and 19 reactions by excluding inert species (e.g., Ar, He). The dataset size is 2 million. The neural network architecture and training procedure are selected in accordance with [10,11]. The network comprises three hidden layers with 800, 400, and 200 neurons, respectively, employs the GELU activation function [31], and is trained with the L_1 loss. Training proceeds in two stages: 2500 epochs at a learning rate of 10^{-4} (batch size 256) for generalization, followed by 500 epochs at 10^{-5} (batch size 32,768) for fine convergence.

The trained neural network is then applied to Cases 1 and 2. The CFD time steps Δt for Cases 1 and 2 are set to 1×10^{-8} s and 1×10^{-9} s, respectively.

3.1.1. Training metrics

Fig. 4(a) shows the evolution of the loss function during training. Convergence is rapid: the training loss decreases from 0.96 to 5.2×10^{-4}, and the validation loss from 0.96 to 5.8×10^{-4}, indicating robust learning without overfitting.

Fig. 4(b) compares one-step Y_{OH} predictions from the ANN against the Cantera reference on the validation set. The horizontal and vertical axes represent the ground-truth values (Cantera) and ANN predictions, respectively. The data points cluster tightly along the diagonal, confirming high-fidelity one-step prediction accuracy.

3.1.2. Results of ODW initiation problems

In this section, the trained ANN is applied to ODW initiation Cases 1 and 2 and compared with the CVODE reference. According to [5], the grid sizes of Cases 1 and 2 are 400 μm and 50 μm, respectively.

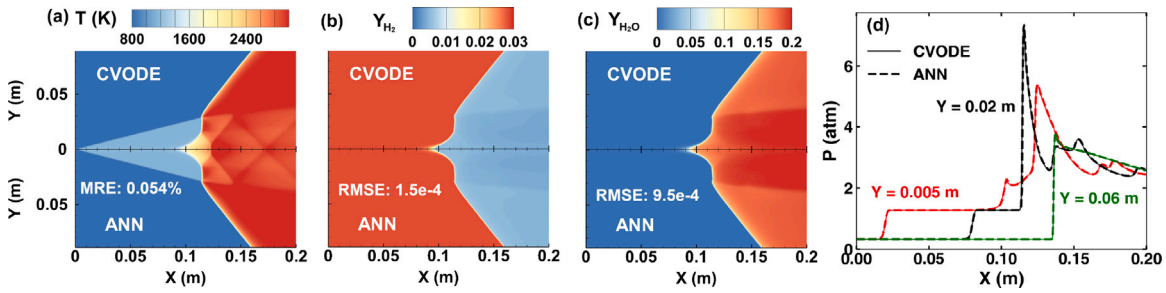


Fig. 5. Comparison of CVODE- and ANN-based simulations of Case 1 (H_2/air abrupt initiation): (a) temperature; (b) Y_{H_2}; (c) Y_{H_2O}; (d) pressure distribution along X at different Y values.

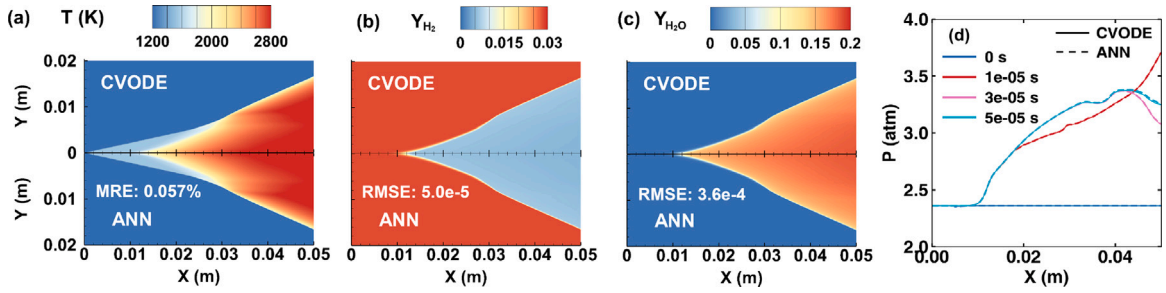


Fig. 6. Comparison of CVODE- and ANN-based simulations of Case 2 (H_2/air smooth initiation): (a) temperature; (b) Y_{H_2}; (c) Y_{H_2O}; (d) pressure distribution along X at $Y = 0$ at different times.

Fig. 5 demonstrates excellent agreement between CVODE and ANN in the predicted wave structures for Case 1. Panels (a)–(c) compare contours of temperature, Y_{H_2}, and Y_{H_2O}; the ANN faithfully reproduces the compression wave, Mach stem, and reflected shocks between the wedge surface and the slip line. Both methods predict a 15° angle between the OSW and the wedge and a 47° angle for the ODW, consistent with Teng et al. [5]. To further quantify the agreement between ANN and CVODE, we evaluate the mean relative error (MRE) and root mean square error (RMSE) of the two-dimensional fields, defined as

$$\mathrm{MRE} = \frac{1}{N}\sum_{i=1}^{N}\left|\frac{q_i^{\mathrm{ANN}} - q_i^{\mathrm{CVODE}}}{q_i^{\mathrm{CVODE}}}\right| \times 100\%, \tag{11}$$

$$\mathrm{RMSE} = \sqrt{\frac{1}{N}\sum_{i=1}^{N}\left(q_i^{\mathrm{ANN}} - q_i^{\mathrm{CVODE}}\right)^2}, \tag{12}$$

where N is the total number of grid points and q denotes the target variable. For temperature and pressure, MRE is reported because it better reflects the relative discrepancy. For mass fractions, RMSE is used instead, since mass fractions of species can be nearly zero and the relative error may become singular there. As shown in Fig. 5(a), the MRE of temperature remains at the order of 0.1%. In Fig. 5(b) and (c), the RMSEs of Y_{H_2} and Y_{H_2O} are only about 1% of their peak value, quantitatively confirming the high accuracy of the ANN. For all two-dimensional simulations presented in this work, we further compute the structural similarity index measure (SSIM), peak signal-to-noise ratio (PSNR), and correlation coefficient R; the corresponding results are summarized in Appendix D.

Fig. 5(d) presents pressure profiles along X at $Y = 0.005$, 0.020, and 0.060 m. At $Y = 0.005$ m, both CVODE and ANN detect the initial pressure rise due to the OSW, followed by multiple oscillations from reflected shock waves. At $Y = 0.020$ m, both methods capture the highest pressure peak associated with the Mach stem downstream of the OSW. At $Y = 0.060$ m, both methods resolve the characteristic ODW pressure rise and subsequent relaxation. Despite the complexity of the wave structures in this case, the ANN and CVODE results are nearly indistinguishable at all heights, confirming accurate capture of ODW initiation dynamics.

Fig. 6 shows the comparison for Case 2 (smooth initiation). Panels (a), (b), and (c) compare temperature, Y_{H_2} and Y_{H_2O} contours, respectively. The wave structure of the smooth initiation consists of a gradual compression, which is considerably simpler than the abrupt transition. CVODE and ANN agree closely on the wave angle. The corresponding MRE and RMSE results also confirm the high accuracy of the ANN predictions. Panel (d) shows the pressure profiles along X on the wedge surface ($Y = 0$) at different transient times. As described in Section 2.1, the OSW in this study is first obtained from a non-reacting calculation and then evolved into an ODW by activating chemical reactions. Panel (d) captures this unsteady OSW-to-ODW transition. The ANN and CVODE results exhibit excellent agreement, capturing both the quasi-steady state and the transient evolution of the smooth initiation process. Similar temporal evolution results for the other cases are presented in Appendix A.

In summary, a single neural network successfully resolves both the abrupt and smooth ODW initiation structures for H_2/air mixtures. For the H_2/air mixture, the one-dimensional ZND-guided sampling strategy can be successfully extended to two-dimensional oblique detonation simulations. For smooth initiation cases, such as Case 2, the conservation relations in Eqs. (8)–(10) describe the jump conditions in the direction normal to a locally planar wave. These relations motivate the use of one-dimensional ZND profiles to sample the relevant thermochemical states. As the transition from OSW to ODW is smooth, the local thermochemical states are well represented within the one-dimensional sampling framework with data-perturbation augmentation (Step 4 of the sampling method). For the abrupt initiation cases, such as Case 1, more complex shock structures may appear in the detonation initiation region. In particular, the Mach stem associated with the normal shock can generate significantly higher pressure and temperature than the regular oblique shock. To capture these extreme states, high-pressure augmentation is introduced in the sampling procedure (Step 2 of the sampling method). By enriching the training data with these high-temperature and high-pressure samples, the relevant thermochemical state space in the two-dimensional flow is adequately covered, enabling the model trained on one-dimensional ZND-based samples to remain accurate in two-dimensional simulations.

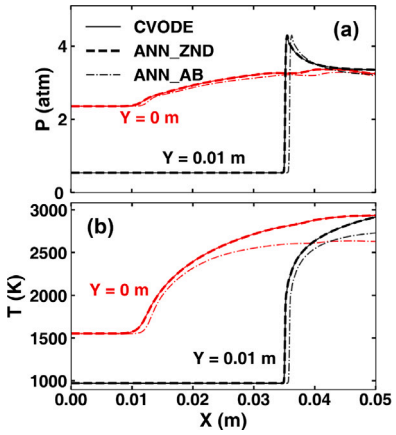


Fig. 7. Ablation study of sampling method on Case 2. (a) Pressure and (b) temperature distributions along X at $Y = 0$ and $Y = 0.01$ m.

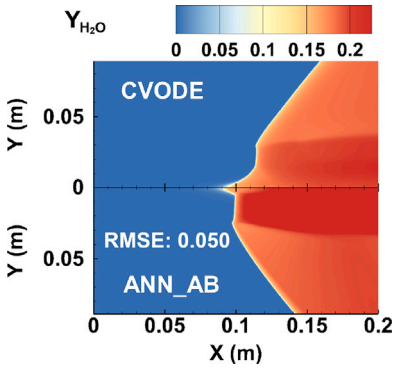


Fig. 8. Ablation study of sampling method on Case 1. Contour of Y_{H_2O} predicted by CVODE and ANN_AB.

3.1.3. *Ablation study of sampling method*

To further demonstrate the advantage of the proposed ZND-guided sampling strategy, we compare it with multi-scale sampling [10–13], a well-established strategy that has proven effective across a wide range of combustion scenarios. The key feature of ZND-guided sampling is that it first constructs initial samples on a low-dimensional manifold associated with the underlying physical problem, and then enriches the dataset by perturbing these samples to improve coverage around the manifold. In contrast, multi-scale sampling draws samples broadly from the full high-dimensional thermochemical state space. As a general-purpose approach applicable to a wide range of combustion problems, it serves as a reasonable baseline for comparison. Following the multi-scale sampling procedure in [10], we generate 2 million samples with $T \in [1000, 4000]$ K, $P \in [0.2, 7]$ atm, $Y_{N_2} \in [0.7, 0.8]$, and $\Delta t \in [8 \times 10^{-10}, 1.2 \times 10^{-8}]$ s. The selected ranges of temperature and pressure are guided by the characteristic upper bounds observed in Cases 1 and 2, where the peak temperature and pressure reach approximately 3200 K and 6 atm, respectively. In addition, the range of Δt is chosen to be consistent with that adopted for the neural network in Section 3.1.2. With these choices, the multi-scale sampling domain provides adequate coverage of the thermochemical states encountered in Cases 1 and 2, thereby ensuring a fair basis for comparison. For the multi-scale sampling strategy, the sampling range of each species is first determined from zero-dimensional simulations. Specifically, the lower and upper bounds of each species mass fraction are extracted from the 0D reaction trajectories, for example, $Y_{OH} \in [10^{-25}, 10^{-1}]$. Then, for each species dimension, random samples are generated within the corresponding range in logarithmic space. In this way, species spanning multiple orders of magnitude can be more evenly represented in the sampled dataset. The sampled thermochemical states are subsequently used to construct the training set for ANN model development. The neural network is then trained using the same strategy described in Section 3.1.

Fig. 7 compares the predictions of CVODE, the neural network trained with ZND-guided sampling (ANN_ZND), and the neural network trained with multi-scale sampling (ANN_AB) for Case 2. Panel (a) shows the pressure distribution, and panel (b) shows the temperature distribution. ANN_ZND is almost indistinguishable from CVODE, whereas ANN_AB exhibits noticeable deviations. In particular, the predicted induction length is 13.6 mm for CVODE and ANN_ZND, while ANN_AB predicts 14.4 mm, corresponding to an error of about 6%. As a result, the overall detonation structure predicted by ANN_AB is shifted downstream. In addition, in the burned-gas region, the temperature predicted by ANN_AB in Fig. 7(b) is lower than that predicted by ANN_ZND.

Fig. 8 compares the Y_{H_2O} contours for Case 1 obtained with CVODE and the ANN_AB trained from multi-scale sampling. As shown previously in Fig. 5(c), the neural network trained with ZND-guided sampling provides accurate predictions of Y_{H_2O}. However, the ANN_AB method fails to reproduce the post-oblique-shock wave structure correctly. In particular, the Mach reflection near the wall cannot remain stationary and instead continues to propagate upstream. Its relatively poor accuracy is also quantitatively reflected by the RMSE, whose value is close to one quarter of the maximum Y_{H_2O}.

In the cases examined, for the same number of training samples, sampling based on a low-dimensional physically relevant manifold yielded more accurate a posteriori predictions than multi-scale sampling over the full thermochemical state space. The advantage of ZND-guided sampling lies in its problem-specific nature: for a target combustion process such as detonation, samples generated around the corresponding physical manifold are more informative and more efficient than broadly distributed samples spanning a wider state space. Multi-scale sampling provides broader coverage, but for a specific application this coverage does not necessarily translate into higher accuracy. When the goal is to train a neural network for a particular combustion scenario, constructing the training set based on the associated physical manifold offers a more economical, efficient, and accurate approach.

3.2. $C_2H_2/O_2/Ar$ *mixtures*

For broader validation, the proposed methodology is applied to $C_2H_2/O_2/Ar$ ODW initiation following Zhang et al. [24]. The unburned gas composition is $X_{C_2H_2} : X_{O_2} : X_{Ar} = 1 : 2.5 : 14.92$ ($\varphi = 1.0$). The chemistry is modeled using a simplified mechanism with 15 species and 21 reactions [32]. Inflow conditions are listed in Table 1. According to [24], the grid sizes of Cases 3 and 4 are 32 μm and 3 μm, respectively.

The dataset size is 3 million. The network comprises three hidden layers with 1600, 800, and 400 neurons; all other training details are identical to those in Section 3.1.

Fig. 9(a1)–(a2) compare the Y_{OH} and pressure contours for Case 3 obtained with CVODE and ANN. The ANN reproduces the main features of the OH distribution, including the elevated-Y_{OH} region along the detonation front and in the post-shock reaction zone, in good agreement with the CVODE result. The pressure contours also capture the characteristic wave structures, including a compression wave (CW) downstream of the OSW induced by chemical heat release and a Mach stem, appearing as a normal detonation wave (NDW), in the abrupt initiation region. Unlike Case 1, a secondary ODW (SODW) appears between the CW and the Mach stem, generating two sets of reflected waves that impinge on the wedge and then converge. Because of the more complex wave system, the MRE and RMSE are higher than those in Fig. 5; however, they still demonstrate the high predictive accuracy of the ANN. Fig. 9(a3) presents the pressure profiles at $Y = 0.002$ and 0.008 m. At $Y = 0.002$ m, both methods capture the pressure peak

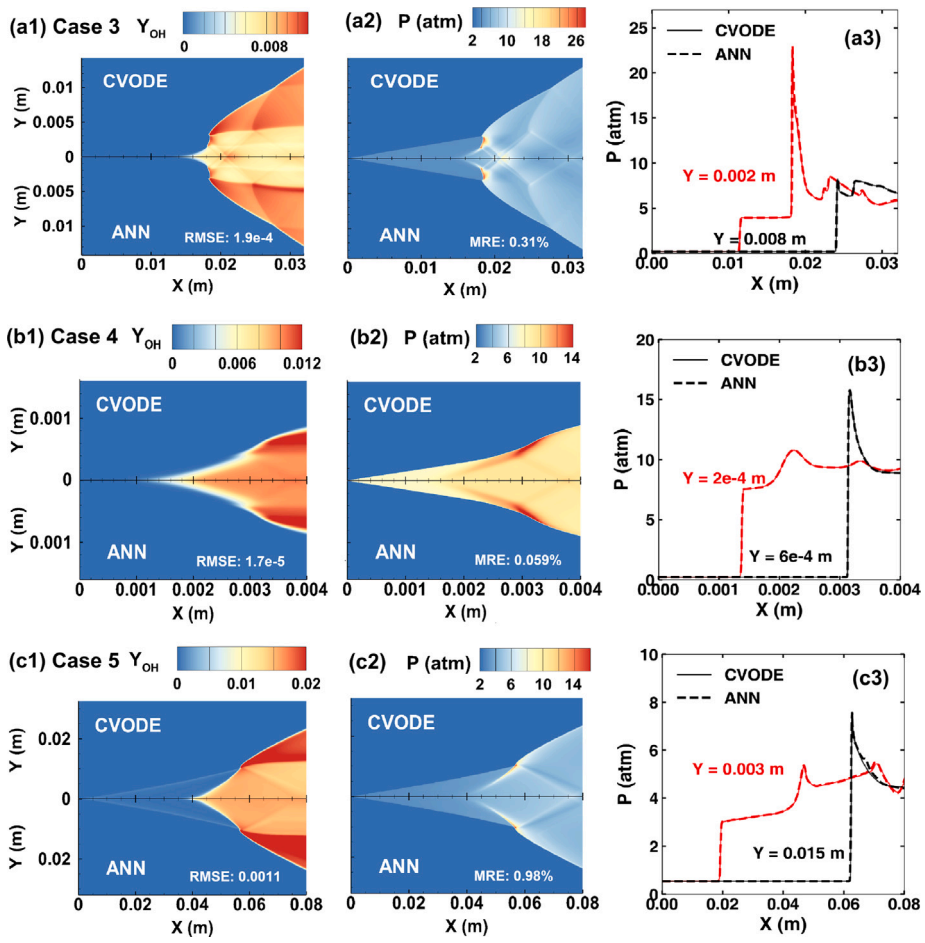


Fig. 9. Comparison of CVODE- and ANN-based simulations for the (Y_{OH}) and pressure contours, together with pressure distributions along X at selected Y locations. (a1)–(a3): Case 3; (b1)–(b3): Case 4; (c1)–(c3): Case 5.

associated with the SODW, the nearby rise induced by a reflected wave, and the two successive increases caused by the converging reflected-wave system. At $Y = 0.008$ m, both methods resolve the two pressure rises associated with the ODW and the transmitted shock. Overall, the ANN predictions agree closely with the CVODE results, indicating that the ANN captures the complex multi-wave interactions in Case 3 with good fidelity.

Fig. 9(b1)–(b2) compare the Y_{OH} and pressure contours for Case 4 obtained with CVODE and ANN. The ANN agrees well with CVODE in both the OH distribution and the overall wave structure, including the reaction zone, the high-Y_{OH} detonation region, and the reflected shock waves. Fig. 9(b3) presents the pressure profiles at different Y locations. At $Y = 2 \times 10^{-4}$ m, both methods capture the pressure rise across the OSW and the two pressure peaks associated with the SODW and the reflected shock waves. At $Y = 6 \times 10^{-4}$ m, both methods reproduce the characteristic pressure increase induced by the ODW. Overall, the ANN predictions remain in close agreement with the CVODE results.

In summary, a single neural network successfully resolves both abrupt and smooth ODW initiation structures for $C_2H_2/O_2/Ar$ mixtures. Additionally, an ablation study for Case 3 further demonstrates the advantage of ZND-guided sampling over direct sampling in the thermochemical space. The results are presented in Appendix E.

3.3. RP3/air mixtures

The proposed methodology is further applied to RP3/air ODW initiation. The chemistry is modeled using a simplified mechanism with 36 species and 155 reactions [33]. Inflow conditions are listed in Table 1.

The dataset size is 4.5 million. The network comprises three hidden layers with 1600, 800, and 400 neurons; all other training details follow Section 3.1. The grid size is 90 μm, and the grid independence test is shown in Appendix B.

Fig. 9(c1)–(c2) compare the Y_{OH} and pressure contours for Case 5 obtained with CVODE and ANN. The ANN shows good agreement with CVODE in both the OH distribution and the pressure field throughout the domain. Due to the increased complexity of the reaction mechanism, the RMSE of Y_{OH} and the MRE of pressure are larger than those in Fig. 5. Nevertheless, the essential wave structures are still captured correctly.

Fig. 9(c3) presents the pressure profiles at $Y = 0.003$ and 0.015 m. At $Y = 0.003$ m, both methods capture the pressure peak across the OSW and the two subsequent pressure rises associated with the SODW and reflected shock waves. At $Y = 0.015$ m, both methods reproduce the characteristic pressure rise associated with the ODW. These results further confirm the close agreement between the ANN and CVODE predictions. The successful application of the neural network methodology to this larger hydrocarbon fuel demonstrates the generality of the approach across different fuel systems and mechanism sizes.

3.4. Computational efficiency

Table 2 summarizes the per-step chemistry computation times. CVODE and CPU-based ANN computations use four Intel Xeon Platinum cores in parallel; GPU-based ANN inference employs a single NVIDIA T4. The reported chemistry time includes only the evaluation of the chemical source terms $\dot{\omega}_\alpha$ and does not include the solution

Table 2
Average chemistry computation time, total time per step, and speedup relative to CVODE.

Case	CVODE		ANN+CPU		ANN+GPU	
	Chemistry (s)	Total (s)	Chemistry (s)	Total (s)	Chemistry (s)	Total (s)
Case 1	1.70	2.34	0.61 (2.8×)	1.25 (1.9×)	0.10 (17×)	0.73 (3.2×)
Case 2	2.12	3.01	0.42 (5.0×)	1.31 (2.3×)	0.10 (21×)	0.98 (3.1×)
Case 3	4.61	6.72	3.55 (1.3×)	5.66 (1.2×)	0.36 (13×)	2.48 (2.7×)
Case 5	22.4	26.2	2.97 (7.5×)	6.76 (3.9×)	0.27 (83×)	4.06 (6.5×)

of Eqs. (1)–(4). In the ANN+GPU configuration, the source terms are evaluated on the GPU, whereas the conservative PDEs are still solved on the CPU. Therefore, the reported chemistry time also includes the CPU–GPU data transfer overhead. However, this communication cost is typically below 1 ms per time step and has a negligible impact on both the total runtime and the chemistry time. For all neural networks considered in this study, the one-step predictions for the ODW problem yield maximum mean absolute errors on the order of 10^{-8} and maximum mean relative errors on the order of 10^{-5} for each species. The relative and absolute tolerances of CVODE are therefore set to 10^{-5} and 10^{-8}, respectively, to ensure a fair comparison. For the H_2/air abrupt initiation (Case 1), the ANN achieves a 3× speedup in chemistry computation time on CPUs and 17× on GPUs. In terms of total runtime per step, the ANN+GPU implementation provides an overall 3.2× speedup. Similar gains are observed across all cases, with GPU deployment reducing the chemistry computation time to approximately 0.1 s per step—substantially alleviating the primary bottleneck in detonation simulations.

The acceleration for the $C_2H_2/O_2/Ar$ ODW initiation (Case 3) is less pronounced than for the H_2/air mixture, primarily because the simplified 21-reaction mechanism already incurs a relatively low CVODE cost. For RP3/air abrupt initiation (Case 5), the ANN achieves a 7.5× speedup in chemistry computation time on CPUs and 83× on GPUs, even when compared against the simplified mechanism. Considering the total simulation cost per step, the ANN+GPU implementation yields an overall 6.5× speedup. This result underscores the increasing advantage of the ANN approach for larger chemical mechanisms and highlights the additional benefit of GPU deployment.

4. Conclusions

A novel Zeldovich–von Neumann–Döring-guided (ZND-guided) low-dimensional manifold approach has been developed to efficiently sample thermochemical data and train artificial neural networks (ANNs) for detonation simulations. This method is applied to construct surrogate models for chemical source terms in oblique detonation wave (ODW) initiation problems. The key findings are summarized as follows:

(1) The ZND structure provides an efficient low-dimensional manifold for detonation data sampling. By computing one-dimensional ZND solutions using Cantera and SDToolbox, augmented with high-pressure, low-temperature, and perturbation-based strategies, a comprehensive dataset is constructed that fully covers the thermochemical space of ODW initiation without requiring expensive two-dimensional simulations. The computational cost of the entire sampling workflow is less than one CPU-hour, in stark contrast to the prohibitive cost of traditional CFD-based dataset generation. The ablation study on the sampling strategy shows that, in the cases examined, the proposed ZND-manifold-based sampling yielded more accurate a posteriori predictions than multi-scale sampling — a strategy known to perform well across a wide range of combustion scenarios — at the same dataset size. For a given application, low-dimensional-manifold-based sampling is therefore more economical and efficient.

(2) The trained ANNs show quantitative agreement with CVODE in the predicted flow-field variables, including temperature, pressure, and species mass fraction distributions, as well as in key physical metrics such as the ODW angle, while the corresponding MRE and RMSE values further confirm the high predictive accuracy. In the present study, one ANN is constructed for each fuel system. The successful validations for H_2/air, $C_2H_2/O_2/Ar$, and RP3/air cases — including both abrupt and smooth initiation types — indicate that the proposed ANN-based chemistry acceleration framework can be applied to different fuels and operating conditions, provided that the network is trained separately for the target reactive system.

(3) Relative to CVODE, the trained ANN also reduces the chemistry cost—by 3× (CPU) and 17× (GPU) for H_2/air, and by up to 7.5× (CPU) and 83× (GPU) for the larger RP3/air mechanism. Consistent with previous machine-learning studies of chemical kinetics, this acceleration is an expected practical benefit of the surrogate approach.

This work presents a practical framework for efficient ODW initiation simulations and offers guidance for integrating neural networks into detonation modeling. Future work will extend this approach to unsteady and three-dimensional detonation scenarios. In addition, this study mainly focuses on the wave-system structure during ODW initiation, while the instability of the ODW front remains an important topic for future investigation. For more complex ODW cases involving boundary layers, front instability, or unsteady inflow conditions, the ZND-guided sampling strategy used here may become less effective as the underlying wave structure departs from the idealized ZND description. In such situations, more tailored data augmentation strategies, combined with physically informed sampling, will likely be required to maintain model robustness across different application scenarios.

CRediT authorship contribution statement

Tinghao Wang: Investigation, Formal analysis, Writing – original draft, Writing – review & editing. **Qizhe Wen:** Validation, Writing – review & editing. **Jie Sun:** Validation. **John Z. Ma:** Validation. **Zhi X. Chen:** Methodology. **Zhi-Qin John Xu:** Conceptualization, Methodology. **Tianhan Zhang:** Conceptualization, Methodology, Supervision, Writing – review & editing. **Jianping Wang:** Resources. **Zheng Chen:** Conceptualization, Supervision, Writing – review & editing.

Declaration of competing interest

The authors declare that they have no known competing financial interests or personal relationships that could have appeared to influence the work reported in this paper.

Acknowledgments

This work is sponsored by the National Natural Science Foundation of China (Nos. 92470127, 52425604) and the Open Research Project of the Key Laboratory of Cross-Domain Flight Interdisciplinary Technology (No. 2025-JCJQ-LC-016-012).

Appendix A. Supplementary data

Supplementary material related to this article can be found online at https://doi.org/10.1016/j.proci.2026.106836.

References

[1] H. Teng, Z. Jiang, Progress in multi-wave structure and stability of oblique detonations, Adv. Mech. 50 (1) (2020) 202002.

[2] J.-L. Cambier, H. Adelman, G.P. Menees, Numerical simulations of an oblique detonation wave engine, J. Propul. Power 6 (3) (1990) 315–323.

[3] C. Viguier, L.F.F.d. Silva, D. Desbordes, B. Deshaies, Onset of oblique detonation waves: Comparison between experimental and numerical results for hydrogen-air mixtures, Symp. (Int.) Combust., [Proc.] 26 (2) (1996) 3023–3031.

[4] D.T. Pratt, J.W. Humphrey, D.E. Glenn, Morphology of standing oblique detonation waves, J. Propul. Power 7 (5) (1991) 837–845.

[5] H. Teng, C. Tian, Y. Zhang, L. Zhou, H.D. Ng, Morphology of oblique detonation waves in a stoichiometric hydrogen–air mixture, J. Fluid Mech. 913 (2021) A1.

[6] Y. Sun, R. Zhu, H. Guo, B. Shi, M. Zhao, Z. Wei, Effects of equivalence ratios on the oblique detonation initiation in ammonia/hydrogen/air mixtures, Combust. Flame 278 (2025) 114279.

[7] F.C. Christo, A.R. Masri, E.M. Nebot, Artificial neural network implementation of chemistry with pdf simulation of H_2/CO_2 flames, Combust. Flame 106 (4) (1996) 406–427.

[8] L.L. Franke, A.K. Chatzopoulos, S. Rigopoulos, Tabulation of combustion chemistry via artificial neural networks (ANNs): Methodology and application to LES-PDF simulation of Sydney flame L, Combust. Flame 185 (2017) 245–260.

[9] T. Ding, T. Readshaw, S. Rigopoulos, W. Jones, Machine learning tabulation of thermochemistry in turbulent combustion: An approach based on hybrid flamelet/random data and multiple multilayer perceptrons, Combust. Flame 231 (2021) 111493.

[10] T. Zhang, Y. Yi, Y. Xu, Z.X. Chen, Y. Zhang, W. E, Z.-Q.J. Xu, A multi-scale sampling method for accurate and robust deep neural network to predict combustion chemical kinetics, Combust. Flame 245 (2022) 112319.

[11] T. Wang, Y. Yi, J. Yao, Z.-Q.J. Xu, T. Zhang, Z. Chen, Enforcing physical conservation in neural network surrogate models for complex chemical kinetics, Combust. Flame 275 (2025) 114105.

[12] J. Yao, Y. Yi, L. Hang, W. E, W. Wang, Y. Zhang, T. Zhang, Z.-Q.J. Xu, Solving multiscale dynamical systems by deep learning, Comput. Phys. Comm. 316 (2025) 109802.

[13] X. Zhang, Y. Yi, L. Wang, Z.-Q.J. Xu, T. Zhang, Y. Zhou, Deep neural networks for modeling astrophysical nuclear reacting flows, Astrophys. J. 990 (2) (2025) 105.

[14] K. Wan, C. Barnaud, L. Vervisch, P. Domingo, Machine learning for detailed chemistry reduction in DNS of a syngas turbulent oxy-flame with side-wall effects, Proc. Combust. Inst. 38 (2) (2021) 2825–2833.

[15] O. Owoyele, P. Pal, ChemNODE: A neural ordinary differential equations framework for efficient chemical kinetic solvers, Energy AI 7 (2022) 100118.

[16] A. Kumar, T. Echekki, Combustion chemistry acceleration with DeepONets, Fuel 365 (2024) 131212.

[17] S. Zhang, C. Zhang, B. Wang, CRK-PINN: A physics-informed neural network for solving combustion reaction kinetics ordinary differential equations, Combust. Flame 269 (2024) 113647.

[18] M. Ihme, W.T. Chung, A.A. Mishra, Combustion machine learning: Principles, progress and prospects, Prog. Energy Combust. Sci. 91 (2022) 101010.

[19] G. Bakalis, M. Valipour, J. Bentahar, L. Kadem, H. Teng, H.D. Ng, Detonation cell size prediction based on artificial neural networks with chemical kinetics and thermodynamic parameters, Fuel Commun. 14 (2023) 100084.

[20] J. Bian, L. Zhou, P. Yang, H. Teng, H.D. Ng, A reconstruction method of detonation wave surface based on convolutional neural network, Fuel 315 (2022) 123068.

[21] A. Baumgart, M.X. Yao, G. Blanquart, Tabulated chemistry approach for detonation simulations, Combust. Flame 272 (2025) 113878.

[22] Z. Chen, R. Yang, Z.X. Chen, Deep neural network-accelerated detonation simulation, in: China National Symposium on Combustion, 2024, 244101.

[23] S. Barwey, S. Prakash, M. Hassanaly, V. Raman, Data-driven classification and modeling of combustion regimes in detonation waves, Flow, Turbul. Combust. 106 (4) (2021) 1065–1089.

[24] Y. Zhang, Y. Fang, H.D. Ng, H. Teng, Numerical investigation on the initiation of oblique detonation waves in stoichiometric acetylene–oxygen mixtures with high argon dilution, Combust. Flame 204 (2019) 391–396.

[25] R. Mao, M. Lin, Y. Zhang, T. Zhang, Z.-Q.J. Xu, Z.X. Chen, *DeepFlame*: A deep learning empowered open-source platform for reacting flow simulations, Comput. Phys. Comm. 291 (2023) 108842.

[26] G.E.P. Box, D.R. Cox, An analysis of transformations, J. R. Stat. Soc. B 26 (1964) 211–243.

[27] D.G. Goodwin, H.K. Moffat, I. Schoegl, R.L. Speth, B.W. Weber, Cantera: An Object-oriented software toolkit for chemical kinetics, thermodynamics, and transport processes, 2024.

[28] EDL, SDToolbox: Numerical Tools for Shock and Detonation Wave modeling, Tech. Rep. FM2018.001, California Institute of Technology, Pasadena, CA, 2023.

[29] H. Li, R. Yang, Y. Xu, M. Zhang, R. Mao, Z.X. Chen, Comprehensive deep learning for combustion chemistry integration: Multi-fuel generalization and a posteriori validation in reacting flow, Phys. Fluids 37 (1) (2025) 015162.

[30] M.P. Burke, M. Chaos, Y. Ju, F.L. Dryer, S.J. Klippenstein, Comprehensive H_2/O_2 kinetic model for high-pressure combustion, Int. J. Chem. Kinet. 44 (7) (2012) 444–474.

[31] D. Hendrycks, K. Gimpel, Bridging nonlinearities and stochastic regularizers with Gaussian error linear units, 2016, CoRR abs/1606.08415. arXiv:1606.08415.

[32] B. Varatharajan, F. Williams, Chemical-kinetic descriptions of high-temperature ignition and detonation of acetylene-oxygen-diluent systems, Combust. Flame 124 (4) (2001) 624–645.

[33] Z. Wang, Y. Zhang, P. Lin, E. Zhao, W. E, T. Zhang, Z.-Q.J. Xu, Deep mechanism reduction (DeePMR) method for fuel chemical kinetics, Combust. Flame 261 (2024) 113286.